A cellulose synthesis inhibitor affects cellulose synthase complex secretion and cortical microtubule dynamics

Julien Renou, Deqiang Li, Juan Lu, Baocai Zhang, Emilie Gineau, Yajin Ye, Jianmin Shi, Aline Voxeur, Elodie Akary, Martine Gonneau, et al.

▶ **To cite this version:**

Julien Renou, Deqiang Li, Juan Lu, Baocai Zhang, Emilie Gineau, et al.. A cellulose synthesis inhibitor affects cellulose synthase complex secretion and cortical microtubule dynamics. Plant Physiology, 2024, 196 (1), pp.124-136. 10.1093/plphys/kiae232 . hal-04688214

HAL Id: hal-04688214
https://hal.science/hal-04688214v1

Submitted on 4 Sep 2024

HAL is a multi-disciplinary open access archive for the deposit and dissemination of scientific research documents, whether they are published or not. The documents may come from teaching and research institutions in France or abroad, or from public or private research centers.

L'archive ouverte pluridisciplinaire **HAL**, est destinée au dépôt et à la diffusion de documents scientifiques de niveau recherche, publiés ou non, émanant des établissements d'enseignement et de recherche français ou étrangers, des laboratoires publics ou privés.

Plant Physiology®

Plant Physiology, 2024, **196**, 124–136
https://doi.org/10.1093/plphys/kiae232
Advance access publication 4 June 2024
Research Article

A cellulose synthesis inhibitor affects cellulose synthase complex secretion and cortical microtubule dynamics

Julien Renou,[1,†] Deqiang Li,[2,3,†] Juan Lu,[2] Baocai Zhang,[3,4] Emilie Gineau,[1] Yajin Ye,[5] Jianmin Shi,[2] Aline Voxeur,[1] Elodie Akary,[1] Anne Marmagne,[1] Martine Gonneau,[1] Magalie Uyttewaal,[1] Herman Höfte,[1] Yang Zhao,[2,6,‡] and Samantha Vernhettes[1,*,‡]

[1]Université Paris-Saclay, INRAE, AgroParisTech, Institute Jean-Pierre Bourgin for Plant Sciences (IJPB), 78000 Versailles, France
[2]Chinese Academy of Sciences Center for Excellence in Molecular Plant Sciences, Shanghai Institute of Plant Physiology and Ecology, Chinese Academy of Sciences, Shanghai 200032, China
[3]University of Chinese Academy of Sciences, Beijing 101408, China
[4]State Key Laboratory of Plant Genomics, Institute of Genetics and Developmental Biology, Chinese Academy of Sciences, Beijing 100101, China
[5]State Key Laboratory of Tree Genetics and Breeding, Co-Innovation Center for Sustainable Forestry in Southern China, Nanjing Forestry University, Nanjing 210037, China
[6]Faculty of Life Science and Technology, Kunming University of Science and Technology, Yunnan 650000, China
*Author for correspondence: samantha.vernhettes@inrae.fr
†These authors contributed equally.
‡These authors are senior authors.
The author responsible for distribution of materials integral to the findings presented in this article in accordance with the policy described in the Instructions for Authors (https://academic.oup.com/plphys/pages/General-Instructions) is Samantha Vernhettes (samantha.vernhettes@inrae.fr).

Abstract

P4B (2-phenyl-1-[4-(6-(piperidin-1-yl) pyridazin-3-yl) piperazin-1-yl] butan-1-one) is a novel cellulose biosynthesis inhibitor (CBI) discovered in a screen for molecules to identify inhibitors of Arabidopsis (*Arabidopsis thaliana*) seedling growth. Growth and cellulose synthesis inhibition by P4B were greatly reduced in a novel mutant for the cellulose synthase catalytic subunit gene *CESA3* (*cesa3*^{pbr1}). Cross-tolerance to P4B was also observed for isoxaben-resistant (ixr) *cesa3* mutants i*xr1-1* and i*xr1-2*. P4B has an original mode of action as compared with most other CBIs. Indeed, short-term treatments with P4B did not affect the velocity of cellulose synthase complexes (CSCs) but led to a decrease in CSC density in the plasma membrane without affecting their accumulation in microtubule-associated compartments. This was observed in the wild type but not in a *cesa3*^{pbr1} background. This reduced density correlated with a reduced delivery rate of CSCs to the plasma membrane but also with changes in cortical microtubule dynamics and orientation. At longer timescales, however, the responses to P4B treatments resembled those to other CBIs, including the inhibition of CSC motility, reduced growth anisotropy, interference with the assembly of an extensible wall, pectin demethylesterification, and ectopic lignin and callose accumulation. Together, the data suggest that P4B either directly targets CESA3 or affects another cellular function related to CSC plasma membrane delivery and/or microtubule dynamics that is bypassed specifically by mutations in CESA3.

Introduction

The cell wall of growing plant cells consists primarily of matrix polysaccharides and cellulose microfibrils. The former are synthesized in Golgi bodies and delivered to the cell surface by secretory organelles, the latter are spun out from plasma membrane-embedded cellulose synthase complexes (CSC) (Albersheim et al. 2012; Lampugnani et al. 2018). During the last decade, major insights into the complexity of cellulose synthesis were obtained from studies combining pharmacology, genetics, cell biology, biochemistry, and structural biology.

CSCs are hexameric complexes, each globule of which consists of a CELLULOSE SYNTHASE CATALYTIC SUBUNIT (CESA) trimer (Purushotham et al. 2020). Three distinct subunits are required for a functional CSC (Desprez et al. 2007; Persson et al. 2007). For primary cell wall synthesis, on which we will concentrate in this study, the CSCs consist of CESA1, 3, and 6-like (Gonneau et al. 2014). Fluorescently tagged CSCs can be observed cycling between intracellular compartments and the plasma membrane, where they follow linear trajectories along cortical microtubules (CMTs), driven by the polymerization of the 18 glucan chains that constitute the cellulose microfibrils. Stresses, including osmotic stress, salt stress, and microbial toxins, can put cellulose synthesis on hold by promoting the rapid (within minutes) accumulation of CSCs in intracellular microtubule-associated compartments (MASCs, also referred to as small cellulose synthase compartments, SmaCCs) (Crowell et al. 2009; Gutierrez et al. 2009; Endler et al. 2015). CSCs also contain other proteins, which comigrate with CESAs in the plasma membrane: the membrane-bound cellulase KORRIGAN (KOR1) (Vain et al. 2014); CELLULOSE SYNTHASE INTERACTOR (CSI/POM2) (Bringmann et al. 2012; Gu et al. 2010), which links CSCs to CMTs; and COMPANION OF CELLULOSE SYNTHASE (CC) proteins (Endler et al. 2015). The latter also binds CMTs, promotes CMT dynamics, and is required for the redirection of CSC to the plasma membrane after their salt stress-induced internalization.

Received November 14, 2023. Accepted April 4, 2024.
© The Author(s) 2024. Published by Oxford University Press on behalf of American Society of Plant Biologists.
This is an Open Access article distributed under the terms of the Creative Commons Attribution-NonCommercial-NoDerivs licence (https://creativecommons.org/licenses/by-nc-nd/4.0/), which permits non-commercial reproduction and distribution of the work, in any medium, provided the original work is not altered or transformed in any way, and that the work is properly cited. For commercial re-use, please contact reprints@oup.com for reprints and translation rights for reprints. All other permissions can be obtained through our RightsLink service via the Permissions link on the article page on our site—for further information please contact journals.permissions@oup.com.

Downloaded from https://academic.oup.com/plphys/article/196/1/124/7687647 by INRA Recherches Forestieres user on 04 September 2024

Genetic analysis has identified numerous other actors, which do not migrate with the CSCs in the plasma membrane but which are required for normal cellulose synthesis in growing cells. This includes the proteins that chaperone the assembly of the CSC in the Golgi apparatus, the delivery of CSCs to the plasma membrane, the anchoring of the microtubules to the plasma membrane, and the internalization of CSCs through clathrin-mediated endocytosis (reviewed by Zhu and McFarlane 2022).

In addition to mutant analysis, chemical genetics is providing insights into the cell biology of cellulose synthesis and cell wall assembly (Surpin et al. 2005). At least 16 distinct cellulose biosynthesis inhibitors (CBIs) of diverse structures have been studied in more or less detail (Larson and McFarlane 2021; Tateno et al. 2016). Plants treated with CBIs phenocopy cellulose-deficient mutant phenotypes including defects in cell elongation, increased radial expansion, and the deposition of callose and lignin in the cell wall (Desprez et al. 2002; Cano-Delgado et al. 2003). Insights into the mode of action of CBIs were obtained by analyzing their impact on CSC components and CMTs and from the study of resistant mutants. Depending on the CBI, one can observe different effects on the CSCs (Tateno et al. 2016). The majority of the CBIs (isoxaben (Paredez et al. 2006; Gutierrez et al. 2009), AE F150944 (Gutierrez et al. 2009), CGA 325'615 (Crowell et al. 2009), thaxtomin A (Bischoff et al. 2009), quinoxyphen (Harris et al. 2012), acetobixan (Xia et al. 2014), Cestrin (Worden et al. 2015), endosidin 20 (ES20) (Huang et al. 2020), C17 (Hu et al. 2016), and flupoxam/triazofenamide (Shim et al. 2018)) promotes the clearance from the plasma membrane of the CSCs and their accumulation in MASCs/SmaCCs (Larson and McFarlane 2021). Some CBIs, instead, promote the accumulation in the plasma membrane of CSCs and reduce (indaziflam, Brabham et al. 2014) or abolish (2,6-dichlorobenzonitrile [DCB], DeBolt et al. 2007b) their motility. Finally, the effect of 2 CBIs (morlin (Debolt et al. 2007a) and cobtorin (Yoneda et al. 2007)) appeared to be limited to the reorientation of microtubules (morlin and cobtorin) and CESA trajectories (morlin) in the plasma membrane. It should be noted that other CBIs can also affect microtubule orientation (Larson and McFarlane 2021; Himmelspach et al. 2003). In general, the uncoupling of CSCs in the plasma membrane from CMTs, through their internalization or in *csi* mutants, has been shown to enhance a mechanosensing feedback loop, promoting the alignment of microtubules along intraorgan stress patterns (Schneider et al. 2022). Such feedback loops make it challenging to distinguish primary from secondary effects of CBI treatments. Among all the CBIs studied, only ES20 was subjected to in vitro binding studies. This showed that ES20 interact with the catalytic domain of CESA6 and not with a mutated version that confers ES20 resistance. ES20 inhibits cellulose synthase activity by reducing CSC motility and secretion and promoting their accumulation in MASCs/SmaCCs (Huang et al. 2020).

Here, we describe a molecule, called P4B, which inhibits cellulose synthesis. The novel mutant *CESA3* allele *cesa3*^{pbr1} and the isoxaben-tolerant mutations in *CESA3* (*ixr1-1* and *ixr1-2*) conferred increased tolerance to P4B. P4B treatment reduced the CSC density in the plasma membrane, by inhibiting their exocytosis, without promoting CSC accumulation in MASCs/SmaCCs. P4B initially did not affect CSC motility in the plasma membrane but disturbed the dynamics of CMTs and favored the formation of EB1a-GFP foci. These observations suggest a mode of action of P4B that is different from previously studied CBIs. Longer term treatments with P4B led to a reduced CSC velocity in a wild type (WT) but not in a *cesa3*^{pbr1} background, a reduced growth anisotropy, the promotion of ectopic lignin and callose deposition, and the prevention of the assembly of an extensible wall.

Results

P4B inhibits cell elongation in Arabidopsis (*Arabidopsis thaliana*) and rice (*Oryza sativa*)

A screen of a library of 12,000 chemicals (Zhao et al. 2007) for growth inhibitory activity on 3-d-old dark-grown *A. thaliana* Columbia (Col)-0 seedlings identified 236 chemicals that caused at least a 70% reduction in hypocotyl length. One of these molecules, 2-phenyl-1-[4-(6-(piperidin-1-yl) pyridazin-3-yl) piperazin-1-yl] butan-1-one, $C_{23}H_{31}N_5O$ (Fig. 1A; Supplementary Fig. S1), hereafter referred to as P4B, was studied in more detail. P4B inhibited dark-grown hypocotyl and root growth with an IC_{50} of 20 μM (Fig. 1, B and C; Supplementary Fig. S2, A and B). Structure–activity analysis of P4B analogs revealed that both the phenyl and ethyl groups are critical for its growth-inhibiting activity on dark-grown seedlings (Supplementary Fig. S1). No difference in sensitivity for P4B was observed for Col-0, Landsberg *erecta* (Ler), or *Wassilevskija* (Ws) accessions (Fig. 1B and Supplementary Fig. S2E). P4B also inhibited root and coleoptile growth of rice (*O. sativa japonica* rice variety 'Zhonghua 11' [Zh11]) seedlings with an IC_{50} of around 50 μM (Supplementary Fig. S3, A and B). Finally, up to 100 μM P4B had no growth effect on the bacterium *Escherichia coli* in liquid culture (Supplementary Fig. S4A) nor on the yeast *Saccharomyces cerevisiae* grown on solid media (Supplementary Fig. S4B). P4B caused reduced cell elongation and increased radial expansion as shown in both Arabidopsis hypocotyls (Fig. 1D, Supplementary Fig. S2, C and D) and rice coleoptiles (Supplementary Fig. S3, C to E).

Increased tolerance to P4B conferred by mutations in *CESA3*

To identify possible cellular targets of P4B, we screened 100,000 EMS-mutagenized Col-0 M2 seeds grown on 50 μM P4B and identified a mutant, named *P4B resistant* (*pbr1*), which showed increased tolerance (IC_{50} = 150 μM) to the hypocotyl growth-inhibiting effect of P4B (Fig. 2, A to C). P4B tolerance of *pbr1* was semidominant and determined by a single locus as shown by the intermediate P4B sensitivity (IC_{50} = 40 μM) of *pbr1* × Col-0 F1 seedlings and the 1:2:1 segregation ratio of the F2 (χ^2 test, P value = 0.325, n = 1207). Using map-based cloning and DNA sequence analysis, we mapped the *pbr1* mutation to the *CESA3* locus (At5G05170) and showed that the mutation causes a L883F replacement in the predicted 4th transmembrane domain of the enzyme (Fig. 2D and Supplementary Fig. S2F). To confirm that this mutation in *CESA3* is causative for the mutant phenotype, we showed that the introduction of a *pCESA3-CESA3* transgene restored P4B sensitivity to the homozygous *cesa3*^{pbr1} mutant (Fig. 2A). In addition, 2 previously described isoxaben-resistant *CESA3* alleles, *cesa3*$^{ixr1-1}$ and *cesa3*$^{ixr1-2}$ (Scheible et al. 2001), but not the *CESA6* allele *cesa6*$^{ixr2-1}$ (Desprez et al. 2002) (Supplementary Fig. S2, G and H) also conferred tolerance to P4B (Fig. 2, C and E). Finally, *cesa3*$^{ixr1-1}$ and *cesa3*^{pbr1}, combined in F1 plants, did not complement each other with respect to the tolerance to P4B-induced growth inhibition (Fig. 2F). Together, the results indicate that the *cesa3*^{pbr1} mutation is causative for the increased tolerance to the growth-inhibiting effects of P4B.

P4B inhibits cellulose synthesis in WT but not in *cesa3*^{pbr1} seedlings

The nature of the P4B-resistant mutants suggests that the molecule is a CBI. This was supported by the 40% to 50% reduction in cellulose content of seedlings grown in the presence of 10 or

Downloaded from https://academic.oup.com/plphys/article/196/1/124/7687647 by INRA Recherches Forestieres user on 04 September 2024

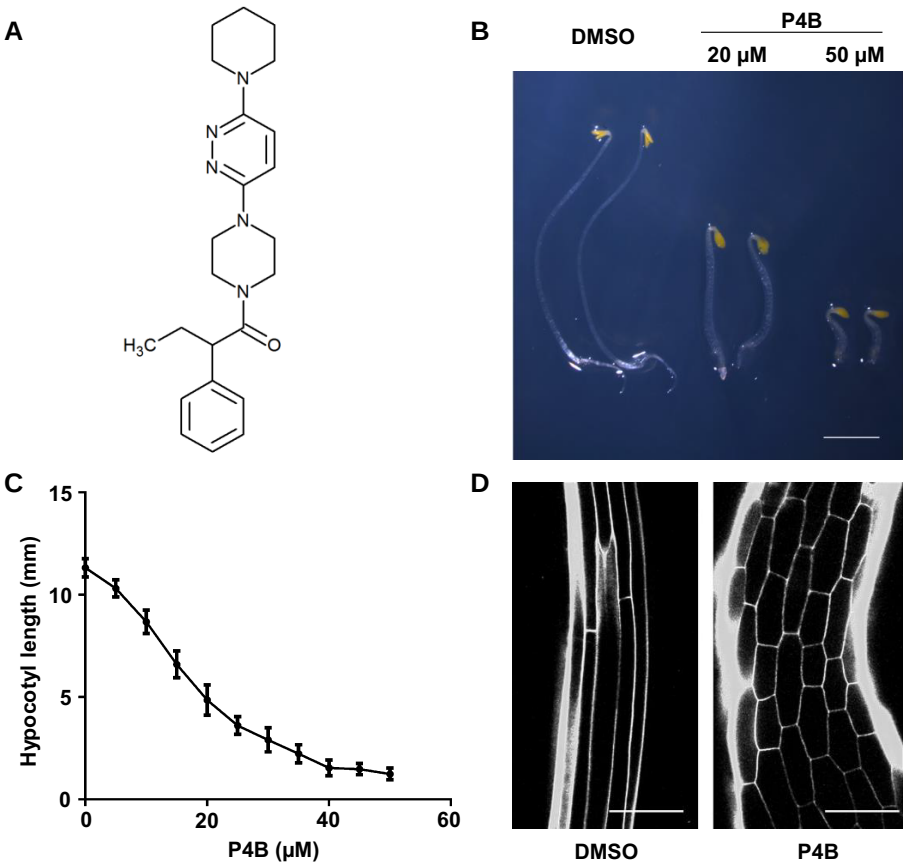

Figure 1. P4B inhibits cell elongation. **A)** The chemical structure of P4B. **B)** Phenotypes of 3-d-old Col-0 seedlings grown in the dark on either 0.5% (v/v) DMSO (left), 20 μM (middle), or 50 μM P4B (right). Scale bar = 2 mm. **C)** Dose–response curve of dark-grown hypocotyl length on P4B. IC50 = 20 μM. Data represent mean ± SD, $n = 20$. **D)** Propidium iodide (PI)-stained 3-d-old etiolated hypocotyl cells treated with 0.5% DMSO or 50 μM P4B. Scale bar = 100 μm.

40 μM P4B relative to DMSO-treated controls, similar to those grown in the presence of 2 nM of the well-characterized CBI isoxaben (Fig. 3A). In addition, P4B inhibited the incorporation of ^{13}C-labeled glucose into the cellulosic fraction in WT but not in *cesa3^{pbr1}* seedlings (Fig. 3B).

P4B inhibits CSC delivery to the plasma membrane

To investigate the mode of action of P4B, we monitored, in the hypocotyl epidermis of dark-grown seedlings, its effect on CSC dynamics using plants expressing *pCESA3-GFP-CESA3* in the partial loss-of-function *cesa3^{je5}* background (Fig. 4 and Supplementary Fig. S5). We found that 5 h P4B treatment reduced the density of GFP-CESA3 punctae, without reducing their velocities in the plasma membrane (Fig. 4, A to C). We were unable to detect an accumulation of CSCs in MASCs/SmaCCs (Supplementary Videos S1 and S2) as has been observed for certain CBIs such as isoxaben (Gutierrez et al. 2009), CGA325'615 (Crowell et al. 2009; Vain et al. 2014), or C17 (Hu et al. 2016), which were shown to rapidly and totally clear GFP-tagged CSCs from the surface and to promote their accumulation in MASCs/SmaCCs. The CSC trajectories in P4B-treated cells also showed a more oblique orientation relative to mock-treated cells (Fig. 4A). This will be addressed below. To investigate the cause of the P4B-induced, decreased density, we monitored the delivery of GFP-CESA3 to the plasma membrane by fluorescence recovery after photobleaching (FRAP). We found that the rate of CSC insertion into the plasma membrane was significantly reduced in P4B-treated cells relative to mock-treated cells (Fig. 4, D and E). This effect appeared to be specific for CSC since P4B did not induce a change in the fluorescence intensity of the plasma membrane protein GFP-LTI6b (Cutler et al. 2000) (Fig. 4, F and G). In addition, P4B treatment did not induce visible changes in the shape of Golgi bodies (marker 22R (Geldner et al. 2009)), TGNs (VHA1-mRFP (Dettmer et al. 2006)), or actin filaments (Kost et al. 1998) nor in Golgi body motility (Supplementary Fig. S6). To assess the effect of the *cesa3^{pbr1}* mutation on CSC behavior, we compared pKOR1-GFP-KOR1 in the leaky *kor^{lit}* and *kor^{lit}/cesa3^{pbr1}* backgrounds, respectively. Given its presence in the CSC complex, GFP-KOR1 can also be used to monitor CSC dynamics (Vain et al. 2014). Like GFP-CESA3, GFP-KOR1 in *kor^{lit}* showed a reduced particle density in the plasma membrane after 5 h P4B treatment accompanied by a more oblique orientation of the trajectories but no change in particle velocity (Fig. 5, A to C). Interestingly, in the *kor^{lit}/cesa3^{pbr1}* background, P4B treatment for 5 h, or even 24 h (see below), did not affect the density or particle velocity nor did it change the direction of the CSC trajectories, relative to mock-treated seedlings except for 5 h mock and P4B-treated samples; we noted that there was a slight increase of around 30 nm/min in the velocity of GFP-KOR1 complexes in kor^{lit}/*cesa3^{pbr1}* background (Fig. 5, D to F, and Supplementary Fig. S7, D to F).

P4B alters CMT dynamics

Given the effect of P4B treatments on the orientation of CSC trajectories, we investigated in more detail its effect on CMT dynamics and orientation. Time-lapse experiments on hypocotyl

Downloaded from https://academic.oup.com/plphys/article/196/1/124/7687647 by INRA Recherches Forestieres user on 04 September 2024

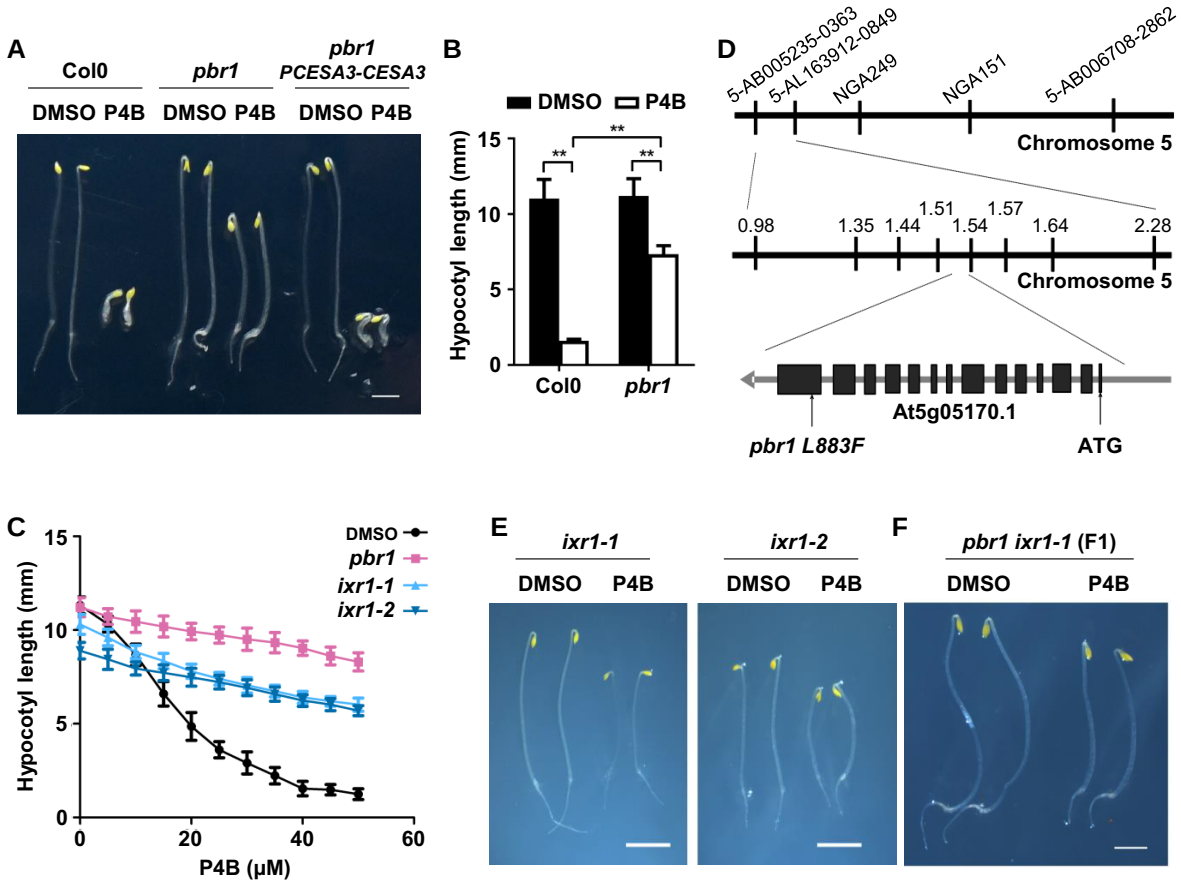

Figure 2. Mutations in CESA3 confer increased tolerance to P4B. **A, B)** Three-day-old phenotypes of WT and *cesa3*^{pbr1} mutant seedlings grown in the dark in the presence of 50 µM P4B or control (0.5% [v/v] DMSO). **A)** Photo of the complementation of *cesa3*^{pbr1} (*pbr1*) phenotype by a *p*CESA3-CESA3 transgene, scale bar = 2 mm. **B)** Quantification of hypocotyl length in presence of 50 µM P4B; bars represent SD, *$P < 0.05$, **$P < 0.01$, Student's *t* test, $n = 20$. **C)** Dose–response curve of dark-grown hypocotyl length of control, *cesa3*^{pbr1}, *cesa3*$^{ixr1-1}$ (ixr1-1) , and *cesa3*$^{ixr1-2}$ (ixr1-2) on P4B. *cesa3*$^{ixr1-1}$ and *cesa3*$^{ixr1-2}$ mutations also confer resistance to P4B. Data represent mean ± SD, $n = 20$. **D)** Genetic mapping and cloning of *pbr1* mutant locus. **E)** Photos of *cesa3*$^{ixr1-1}$ and *cesa3*$^{ixr1-2}$ dark-grown seedlings on either DMSO or 50 µM P4B, scale bar = 2 mm. **F)** Photo of *cesa3*^{pbr1}/*cesa3*$^{ixr1-1}$ F1 cross grown on either DMSO or 50 µM P4B, scale bar = 2 mm.

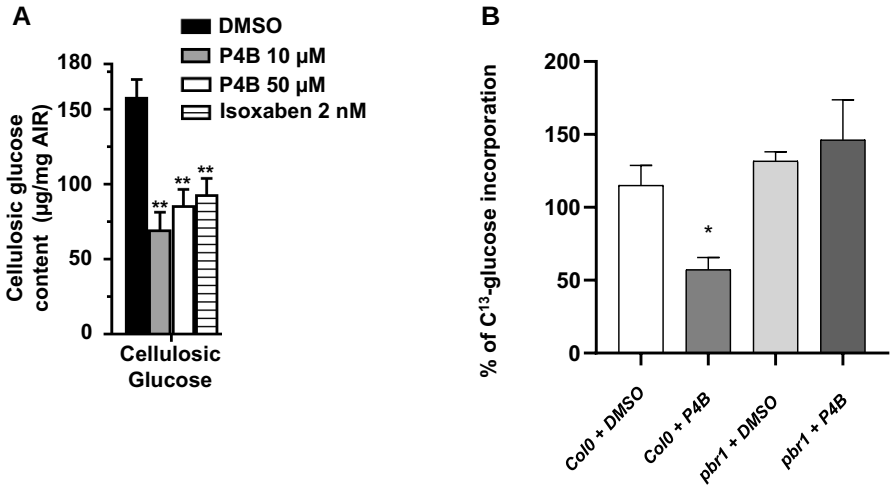

Figure 3. P4B is a cellulose synthesis inhibitor. Col0 Arabidopsis seedlings were grown for 3 d in the dark in the presence of buffer only, P4B (10 µM or 50 µM), or isoxaben (2 nM). **A)** Cellulosic glucose content (in µg/mg AIR). **B)** Ratio between 5 and 24 h of the amount of C^{13}-glucose incorporation into crystalline cellulose in Col0 and *cesa3* ^{pbr1} (*pbr1*) mutants treated with DMSO or 50 mM P4B. Bars represent SD, *$P < 0.05$, **$P < 0.01$, Student's *t* test, $n = 4$ for each experiment.

epidermal cells expressing EB1a-GFP revealed 2 spatially separated subpopulations of EB1a-GFP: 1 population of immobile foci at the plasma membrane and a mobile population labeling the plus-ends of microtubules (Fig. 6, A and B, and Supplementary Fig. S8, A and B). P4B treatment for 5 h reduced the speed of the microtubule plus-ends and increased the size of the

Downloaded from https://academic.oup.com/plphys/article/196/1/124/7687647 by INRA Recherches Forestieres user on 04 September 2024

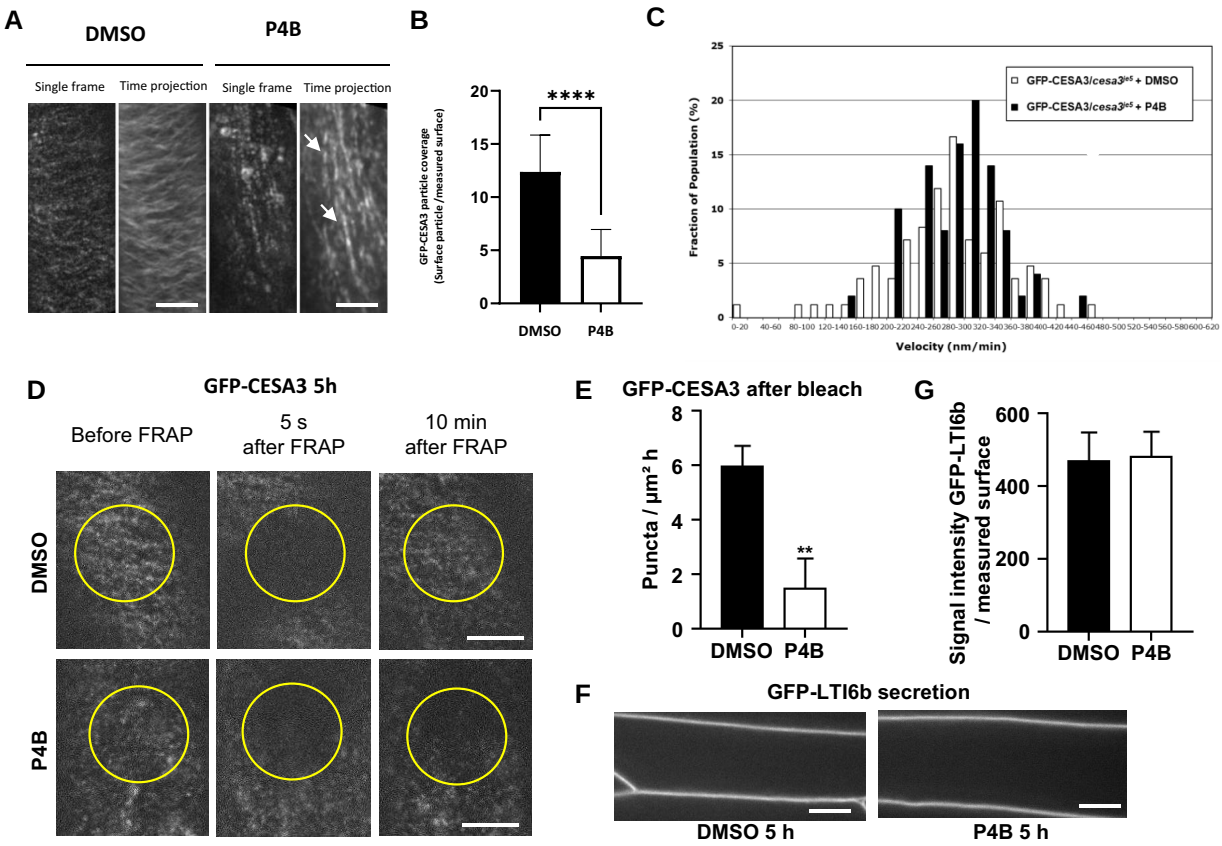

Figure 4. P4B inhibits GFP-CESA3 delivery and affects its plasma membrane organization. Three-day-old dark-grown seedlings of GFP-CESA3/*cesa3*^{je5} (**A** to **E**) or LTI6-GFP (**F**, **G**) were transferred to Arabidopsis liquid medium containing 0.5% (*v*/*v*) DMSO or 100 µM P4B and incubated for 5 h. **A, B)** Representative single frame and time-projected images (10 min, 61 frames) of GFP-CESA3/*cesa3*^{je5} in 5 h mock and P4B-treated hypocotyl cells. Arrowheads indicate brighter punctae. **B)** Coverage of GFP-CESA3 particles in DMSO and P4B-treated hypocotyl cells after 5 h treatment. Error bars represent SE. ****$P < 0.0001$ Student's *t* test, $n = 92$ cells in each treatment. **C)** Distribution of velocities of GFP-CESA3/*cesa3*^{je5} in 5 h mock (mean velocity: 260 ± 53 nm/min) and P4B-treated (mean velocity: 276 ± 60 nm/min) hypocotyl cells. **D)** Representative time-course images of photobleaching of GFP-CESA3 in 5 h mock and treated P4B hypocotyl cells. **E)** Quantification of the rate of GFP-CESA3 recovery in the plasma membrane after photobleaching in 5 h mock and P4B-treated hypocotyl cells. The graph summarizes 3 independent experiments. Error bars represent SE. **$P < 0.01$ Student's *t* test, $n = 15$ cells in each treatment (1 cell imaged per seedling). **F)** Representative images of the plasma membrane marker, GFP-LTI6b, in mock and P4B-treated plants after 5 h treatment. **G)** Quantification of signal intensity from GFP-LTI6b signal represented in (**F**). Error bars represent SE $n = 30$ cells in each treatment. Scale bars = 10 µm.

quasi-immobile population (Fig. 6, A and B, Supplementary Videos S3 and S4). This type of immobile EB1 foci has been previously described (Chan et al. 2003; Barton et al. 2008). Measurement of CMT polymerization dynamics in GFP-TUA6-expressing cells after 5 h P4B treatment confirmed the decrease (~35%) in elongation rate at the plus-end and revealed an unaltered shrinkage rate (Fig. 6, C to E), associated with an increase and a decrease in the % of time spent growing or shrinking, respectively. P4B also promoted the bundling of GFP-MAP4-labeled CMTs indicated by the stronger labeling of the microtubules relative to the mock control (Fig. 6, F and G). P4B treatment for 5 h also induced a reorientation from transverse to oblique of RFP-MBD-tagged CMTs and GFP-CESA3-tagged CSC trajectories, which correlated with the inhibition of hypocotyl elongation (Fig. 7, A and B). The latter data also showed that P4B did not affect the microtubule–CSC interaction.

Taken together, the earliest observable cellular effects of P4B treatments were the reduced CSC delivery to the plasma membrane and the altered dynamics of the CMTs, without an inhibition of the motility of the CSCs in the plasma membrane.

Long-term effects of P4B treatment

In contrast to 5 h treatments, 24 h and longer treatments with P4B greatly reduced the velocity of EB1a-GFP comets (Supplementary Fig. S8), GFP-CESA3- (Supplementary Fig. S5) and GFP-KOR1-tagged CSCs in the plasma membrane (Supplementary Fig. S7), and GFP-CESA3-tagged Golgi bodies but did not slow down in the presence of P4B but showed a tendency to aggregate (Supplementary Figs. S5 and S9). Also, after 24 h P4B treatment, GFP-CESA3 trajectories and RFP-MBD-labeled microtubules remained parallel suggesting that the treatment did not interfere with the CMT–CSC interaction. Again, in the *kor*^{lit}/*cesa3*^{pbr1} background, the 24 h P4B treatment did not affect the GFP-KOR1 particle density in the plasma membrane nor the particle velocity or directionality relative to mock-treated seedlings (Supplementary Fig. S7). P4B also favored the accumulation of ectopic lignin and callose (Supplementary Fig. S10, A and B); the latter was also reflected in the higher amounts of noncellulosic glucose in the cell walls (Supplementary Fig. S10C). The treatment also induced other changes in the cell wall composition, such as the increased galactose and xylose levels and the reduced methylesterification levels of an acetylated fraction of the pectic polymer homogalacturonan (Supplementary Fig. S10D), as shown by the reduction in methylesterified oligosaccharides ($GalA_5Me_2$ and $GalA_4Me$) and the increase in GalA3 and acetylated oligosaccharides ($GalA_3Ac$ and $GalA_4Ac$) released by endo-polygalacturonase treatment of cell wall preparations. The latter effects were not observed in *cesa3*^{pbr1} treated or not with P4B.

Downloaded from https://academic.oup.com/plphys/article/196/1/124/7687647 by INRA Recherches Forestieres user on 04 September 2024

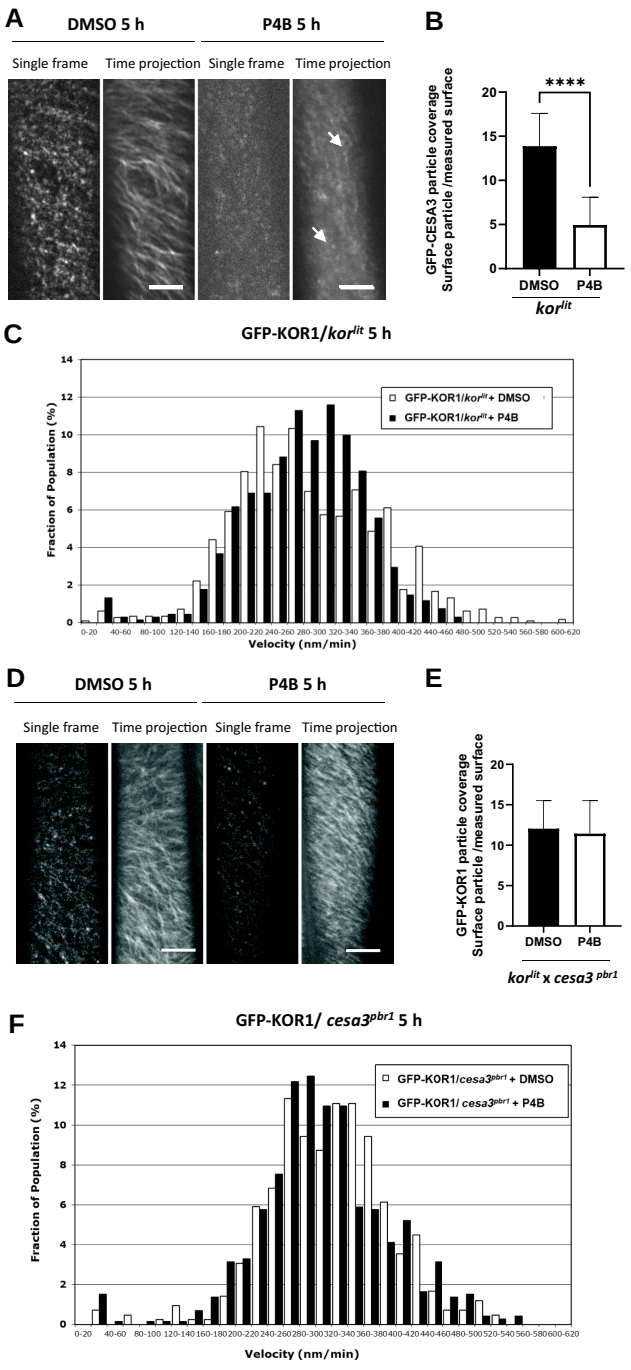

Figure 5. In *cesa3*^{pbr1} mutant, the density and the velocity of CSC is restored. Three-day-old dark-grown seedlings of GFP-KOR1/*kor*^{lit} **(A** to **C)** or GFP-KOR1/*kor*^{lit}x*cesa3*^{pbr1} **(D** to **F)** were transferred to Arabidopsis liquid medium containing 0.5% DMSO or 100 μM P4B and incubated for 5 h. **A)** Representative single frame and time-projected images (10 min, 61 frames) of GFP-KOR1 in 5 h mock- and P4B-treated *kor*^{lit} hypocotyl cells. **B)** Coverage of GFP-KOR1 particles in DMSO- and P4B-treated *kor*^{lit} hypocotyl cells after 5 h treatment. Error bars represent SE. $^{****}P < 0.0001$ Student's *t* test, $n = 115$ cells in each treatment. **C)** Distribution of GFP-KOR1 velocities in 5 h mock (mean velocity: 266 ± 73 nm/min) and P4B-treated hypocotyl cells (mean velocity: 258 ± 77 nm/min). Arrows indicate brighter puncta. **D)** Representative single frame and time-projected images (10 min, 61 frames) of GFP-KOR1/*kor*^{lit}x*cesa3*^{pbr1} in 5 h mock- and P4B-treated hypocotyl cells. **E)** Coverage of GFP-KOR1 particles in DMSO- and P4B-treated *kor*^{lit}x*cesa3*^{pbr1}hypocotyl cells after 5 h treatment. Error bars represent SE, $n = 115$ cells in each treatment. **F)** Distribution of velocities of GFP-KOR1 in 5 h mock- (mean velocity: 297 ± 77 nm/min) and P4B-treated *kor*^{lit}x*cesa3*^{pbr1} hypocotyl cells (mean velocity: 289 ± 83 nm/min). Scale bars = 10 μm.

Finally, we used transmission electron microscopy to study the cell walls in growing hypocotyls (Supplementary Fig. S11). Whereas in most cells, wall deposition is coupled to cell growth, in the epidermis of dark-grown hypocotyls, massive wall deposition takes place in the external wall during a slow isotropic growth phase. This leads to the formation of an over 1-μm-thick multilamellated, but highly extensible, cell wall, which during a subsequent rapid anisotropic growth phase undergoes significant thinning (Refrégier et al. 2004; Derbyshire et al. 2007). In this context, we studied the impact of P4B on wall deposition and remodeling in WT and *cesa3*^{pbr1} at 3 time points marking the transition between slow isotropic growth (42 to 48 h) and rapid anisotropic growth (48 to 72 h) (Pelletier et al. 2010; Peaucelle et al. 2015). Over the time period studied, hypocotyl elongation growth was comparable in mock-treated Col-0 and *cesa3*^{pbr1} (Supplementary Fig. S12). In the presence of 50 μM P4B, however, elongation growth was greatly reduced for Col-0 and slightly reduced for *cesa3*^{pbr1}. As shown previously (Refrégier et al. 2004), in mock-treated Col-0 seedlings, walls were thickest with a multilamellated architecture at 42 h and became substantially thinner at 72 h (Supplementary Fig. S11, A and B), while the outer surface of the cell wall became more undulated. This undulation may reflect a gradient in wall elasticity, where, upon removal of the turgor pressure during the sample preparation, more elastic inner layers of the wall contract, causing the less elastic outer layers to buckle. The absence of buckling at 42 h suggests that, at this stage, inner and outer wall layers had a comparable elasticity (Supplementary Fig. S11C). In the presence of P4B, Col-0 seedlings showed a thinner wall, which lacked the pronounced layered architecture of the mock control. Interestingly, in contrast to the mock control, the thickness of the walls of P4B-treated cells increased between 42 and 48 h, to remain stable at 72 h, and with no change in the degree of buckling (Supplementary Fig. S11, A to C). These results indicate that P4B slowed down cell wall deposition during the slow isotropic cell growth phase and prevented the thinning of the cell wall that is normally associated with the rapid anisotropic growth phase. The reduced buckling suggests that P4B prevented the stiffening of older wall layers and/or promoted the stiffening of newly deposited layers. In mock-treated *cesa3*^{pbr1}, the cell wall was thinner relative to Col0 at 42 h, indicating that, even in the absence of P4B, cell wall accumulation was reduced in the mutant. Despite their reduced thickness, however, the walls maintained their growth capacity, as shown by the normal growth rate and the further thinning between 48 and 72 h. P4B treatment slightly reduced the wall thickness at 42 h relative to the mock-treated mutant, but no such differences were seen at 48 and 72 h consistent with the P4B tolerance of the mutant. Also, wall maturation appeared to occur normally for *cesa3*^{pbr1} both in the presence or absence of P4B, as seen by the gradual increase in the buckling of outer cell wall layers. In conclusion, P4B interfered with the assembly of an extensible cell wall and the *cesa3*^{pbr1} mutation bypassed this effect.

Discussion

This study identified P4B as a new small molecule inhibitor of cellulose synthesis, demonstrated by its inhibitory effect on cellulose accumulation and the increased tolerance to the molecule conferred by 3 mutations in CESA3. P4B affects seedling growth both in Arabidopsis and rice with IC50 values of around 20 and 50 μM, respectively, without perturbing yeast or bacterial growth. Structure–function analysis of the molecule shows that the piperidinyl and ethyl groups are essential for its growth-inhibiting

Downloaded from https://academic.oup.com/plphys/article/196/1/124/7687647 by INRA Recherches Forestieres user on 04 September 2024

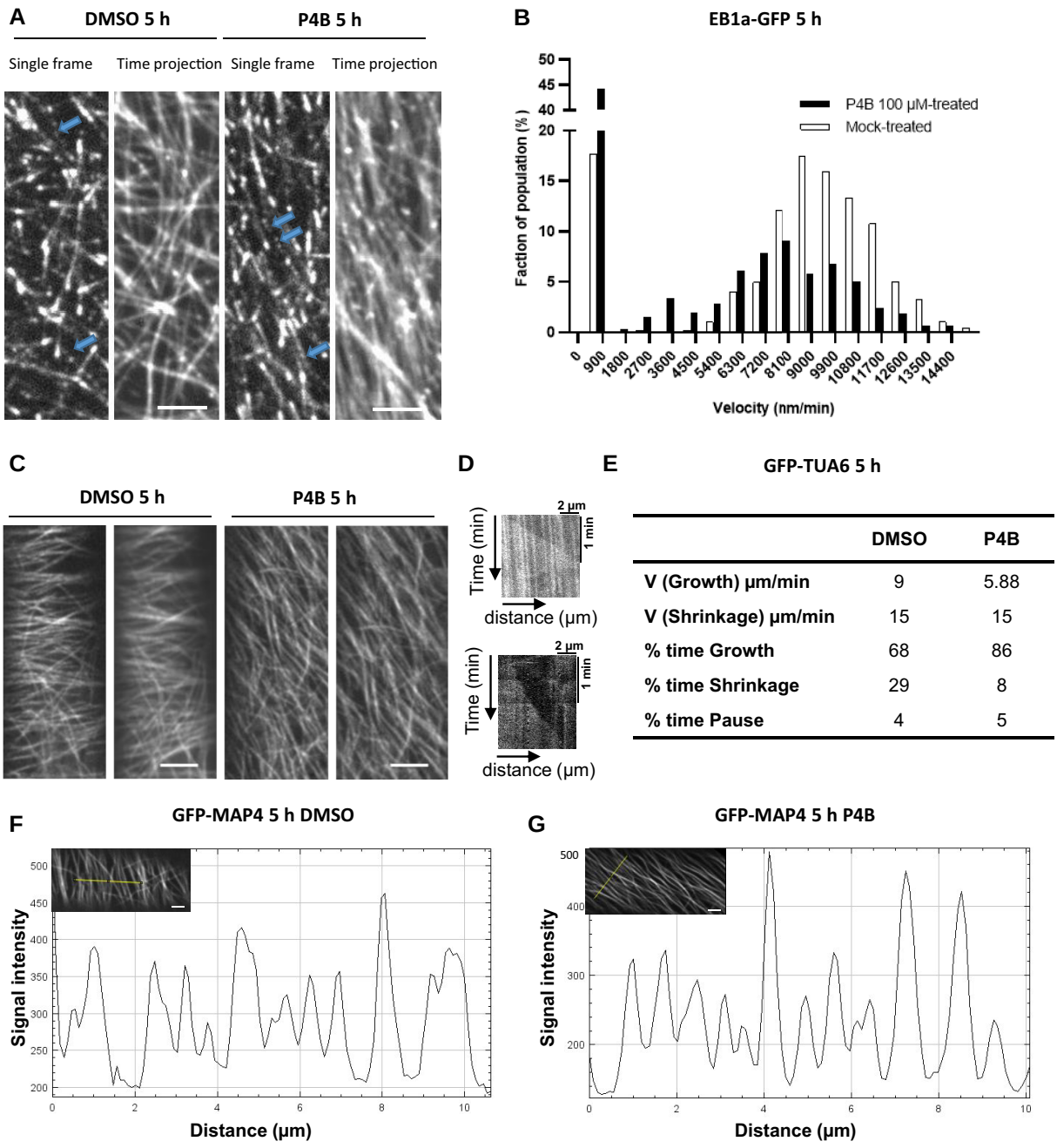

	DMSO	P4B
V (Growth) µm/min	9	5.88
V (Shrinkage) µm/min	15	15
% time Growth	68	86
% time Shrinkage	29	8
% time Pause	4	5

Figure 6. P4B affects the dynamic instability of CMT. Three-day-old dark-grown seedlings of EB1a-GFP **(A** to **B)**, GFP-TUA6 **(C** to **E)**, and GFP-MAP4 **(F**, **G)** were transferred to Arabidopsis liquid medium containing 0.5% DMSO or 100 µM P4B during 5 h. **A)** Representative single frame and time-projected images (2 min, 120 frames) of the EB1a-GFP marker in epidermal cells. Arrows indicate immobile foci. **B)** Distribution of the velocities of EB1 comets in epidermal cells (data from 40 cells from 20 plants with 629 measurements in mock samples and with 647 measurements in P4B-treated samples) calculated from kymographs extracted from the time series realized during these experiments. **C)** Representative single frame and time-projected images (2 min, 120 frames) of the GFP-TUA6 marker in epidermal cells after 5 h treatment. **D)** Representative image of a kymograph obtained from the time series realized during these experiments after mock (upper panel) and P4B (lower panel) treatment (2 min, 120 frames). **E)** Measurements of single CMT of plus-end growth phases in vivo. Measurements of 20 CMT in 5 cells in mock and P4B-treated samples. **F)** Representative image of GFP-MAP4 marker after 5 h DMSO treatment and the corresponding profile of intensity peaks along the line. **G)** Representative image of GFP-MAP4 marker after 5 h P4B treatment and the corresponding profile of intensity peaks along the line. Scale bars = 10 µm.

activity. Given the relatively high IC_{50} value (10^4 times higher than that of isoxaben), its use as a broad-spectrum herbicide would require the isolation of more effective analogs.

What is the mode of action of P4B? Like other CBIs, P4B induced numerous changes in seedlings, but to distinguish primary from secondary effects, it is important to focus on short-term effects (Desprez et al. 2002; Cano-Delgado et al. 2003; Bischoff et al. 2009; Hu et al. 2016). A 5 h treatment did not entail the clearance of GFP-CESA3 or GFP-KOR1 from the plasma membrane and accumulation in MASCs/SmaCCs as described for most of the reported CBIs (Paredez et al. 2006; Crowell et al. 2009; Gutierrez et al. 2009; Bischoff et al. 2009; Harris et al. 2012; Xia et al. 2014; Worden et al. 2015; Hu et al. 2016; Shim et al. 2018; Huang et al. 2020). The treatment also did not change the GFP-CESA3 or GFP-KOR1 motility. Given that cellulose polymerization drives the CSC movement in the plasma membrane, this suggests that P4B did not directly

Downloaded from https://academic.oup.com/plphys/article/196/1/124/7687647 by INRA Recherches Forestieres user on 04 September 2024

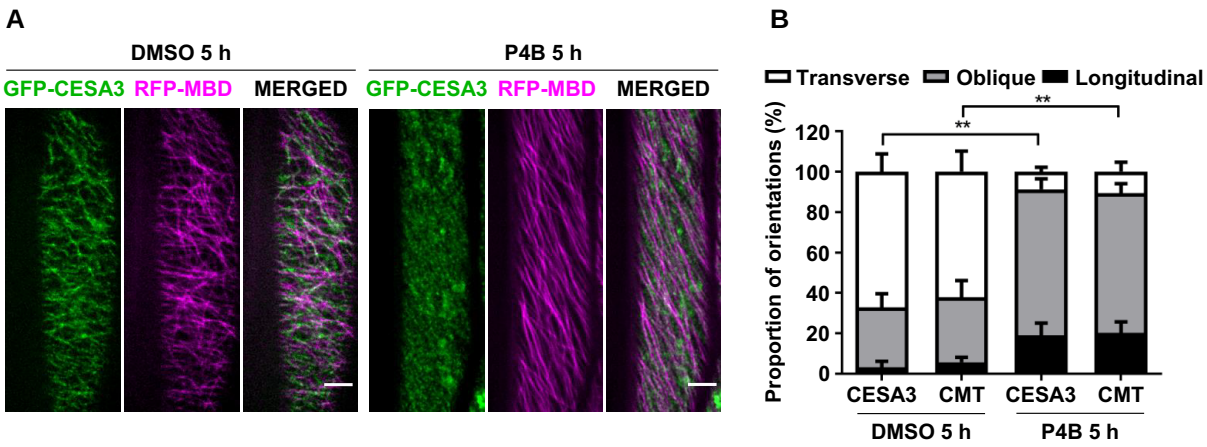

Figure 7. P4B promotes microtubule reorientation but does not affect microtubule–CSC interaction. Single frame images **(A)** and quantification of the angle of GFP-CESA3 trajectories or CMTs **(B)** of epidermal cells of 3-d-old etiolated hypocotyls expressing GFP-CESA3 and RFP-MBD after 5 h mock or 100 μM P4B treatment. Scale bar = 10 μm. Error bars represent SE. **$P < 0.01$ Student's t test, $n = 15$ cells in each treatment.

inhibit the enzymatic activity of the complex. A 5 h P4B treatment instead did reduce the rate of CSC exocytosis, as described for ES20 (Huang et al. 2020), induced the CMTs to adopt a more oblique orientation, and reduced their plus-end growth rates. The 3 P4B-tolerant alleles in *CESA3* suggest that the decrease in cellulose synthesis is causative for most if not all other phenotypes, in which case the changes in CMT dynamics may be the consequence of changes in the supracellular stress patterns associated with changes in cell expansion rates, which are known to feed back onto the CMT orientation through an unknown mechanism (Hamant et al. 2019). The 3 mutations conferring P4B tolerance map to transmembrane domain (TM)4 (*cesa3*^{pbr1}), TM7 (*cesa3*$^{ixr1-1}$), and the gating loop (*cesa3*$^{ixr1-2}$) of CESA3. It is plausible that these mutations at different locations within the molecule directly or indirectly affect the binding of P4B to CESA3. In this scenario, the lack of P4B resistance of the *cesa6*$^{ixr2-1}$ mutant suggests that P4B has a binding pocket that is different from that of isoxaben. Alternatively, the mutations could prevent the interaction of CESA3 with some other molecule that changes upon P4B treatment, for instance, a regulator of CMT dynamics that interacts with CESA3 and controls the plasma membrane insertion of CSCs.

Besides triggering the inhibition of cellulose accumulation, long-term treatments with P4B like with other CBIs, induced other changes in the cell wall, including changes in the outer cell wall architecture of hypocotyl epidermis cells, ectopic lignin and callose accumulation, an increase in xylose- and galactose-containing polymers, and a reduction in pectin methylesterification. These changes are most likely in part related to P4B-induced cell wall damage responses induced by the inhibition of cellulose. A future challenge will be to understand these complex interrelationships, and P4B may be a valuable tool in this endeavor.

Materials and methods

Plant materials

EMS Arabidopsis mutant lines for *cesa3*$^{ixr1-1}$ and *cesa3*$^{ixr1-2}$ (Heim et al. 1989; Scheible et al. 2001) were purchased from the Arabidopsis Biological Resource Center. *Cesa6*$^{ixr2-1}$ is from (Desprez et al. 2002). The Wave 22R (Geldner et al. 2009), VHA-A1-mRFP (Dettmer et al. 2006), GFP-MAP4 (Marc et al. 1998), GFP-mTalin (Kost et al. 1998) GFP-LTI6b (Cutler et al. 2000), and EB1a-GFP (Chan et al. 2007) were kindly provided by N. Geldner, K. Schumacher, M. Pastuglia, S. Cutler, and J. Chan. The GFP-CESA3, GFP-TUA6, GFP-KOR1, and the dual marker line expressing GFP-CESA3 and mRFP-MBD were described previously (Chan et al. 2007; Desprez et al. 2007; Crowell et al. 2009; Vain et al. 2014). The GFP-TUA6 and GFP-KOR1 were crossed into *cesa3*^{pbr1}. The presence of *CESA3*^{pbr1} mutation was verified by a CAPS marker using primers *pbr1* CAPS F and *pbr1* CAPS R and subsequent HinfI digestion (Supplementary Table S1).

Chemical genetics screens

Novel molecules with cell growth inhibitory activities were uncovered from chemical genetic screenings using etiolated 3-d-old Col-0 seedlings against a 12,000 structurally diverse synthetic small molecule chemical library purchased from the Life Chemical Incorporation (Ontario, Canada). The chemical screenings were carried out in 96-well plates as described (Zhao et al. 2007) except the chemical concentration used in the initial screen was 100 μM. The plant chemical genetics phenotypes were observed and imaged using a SZX16 dissecting microscope (Olympus).

Growth conditions and chemical treatment

Surface sterilized Arabidopsis seeds were suspended with 0.1% (w/v) agar, plated on 0.7% solidified agar medium containing 1/2 MS salts (Sigma-Aldrich) with 1% sucrose for root experiments or without sucrose for hypocotyl experiments, and then cold-treated at 4 °C for 3 d. For root measurements, seedlings were vertically grown at 22 °C under 16 h light/8 h dark conditions. For hypocotyl measurements, seeds were exposed to fluorescent white light (150 mmol/m^2/s) for 6 h, and then, plates were wrapped in aluminum foil, and seedlings were vertically grown at 22 °C under constant dark. Seedlings were scanned and photographed using a SZX16 dissecting microscope (Olympus). The age of the seedlings was defined with respect to the end of stratification. For confocal microscopy, 3-d-old seedlings on 1/2 MS agar plate were transferred on liquid media containing DMSO or P4B, for further growth for 5 h (as a short-term treatment) or 24 h (as a long-term treatment).

For chemical genetics assay on seedlings of rice (*O. sativa* L.), rice dry seeds of 'Zhonghua 11,' a japonica cultivar, were surface sterilized with 10% (v/v) NaClO solution for 10 min and washed with sterilized distilled water for 3 times. Sterilized rice seeds

Downloaded from https://academic.oup.com/plphys/article/196/1/124/7687647 by INRA Recherches Forestieres user on 04 September 2024

were placed on 9 cm wide petri dishes containing water, germinated at 28 °C for 2 d under dark condition and then 37 °C grew for another day, and then transferred to 12-well plates, of which each well was filled with 2 mL distilled water containing either 1% DMSO or different concentrations of P4B. Seedlings were photographed after 3 d growth at 28 °C under a 16/8 h light/dark cycle. Measurement of hypocotyl, root, or coleoptile length was performed using ImageJ (W.S. Rasband; National Institutes of Health).

E. coli growth and *S. cerevisiae* growth assay

For *E. coli* growth assay, a single colony of *E. coli* DH5α was inoculated in 3 mL of Luria-Bertani (LB) liquid medium and incubated overnight at 37 °C on a shaker (Thermo). Then 20 μL of the culture was inoculated in 4 mL LB liquid medium containing DMSO or different concentrations of P4B and grew on the shaker at 37 °C. The optimal density value was measured every hour from 0 to 8 h after incubation using a SmartSpec Plus spectrometer (Biorad).

For *S. cerevisiae* growth assay, a single colony of *S. cerevisiae* that has grown for 48 h on solid medium was then inoculated and suspended in 25 μL of sterile water. A total of 2.5 μL of the serially diluted (1:1, 1:10, 1:100, 1:1,000) suspensions of *S. cerevisiae* was separately spotted onto petri plates of solid yeast extract peptone dextrose (YPD) medium containing DMSO or various concentrations of P4B. Plates were incubated for 48 h at 30 °C before photos were taken.

Callose and lignin staining

Col-0 and *cesa3*^{pbr1} seedlings were grown on either 0.5% (*v*/*v*) DMSO or 50 μM P4B for 3 d in the dark. For callose staining, the seedlings were merged in Eppendorf tubes containing 400 μL 0.1 mg/mL Aniline Blue Fluorochrome (Sigma-Aldrich) solution and stained for 1 h under dark. Then samples were spread on slides before observation using a BX51TRF microscope (Olympus) under UV light. For lignin staining, seedlings were put on slides on which phloroglucinol in a 20% (*v*/*v*) hydrochloric acid solution was added. After 5 min staining, samples were covered with a cover slip and then observed under a SZX16 dissecting microscope (Olympus) in bright field (BF) mode.

Cell wall monosaccharide composition analysis and crystalline cellulose

The analyses of polysaccharides were performed on alcohol insoluble residue (AIR) from 3-d-old seedlings grown in the dark. Thirty seedlings ground were washed twice with ethanol 96% and rinsed twice with acetone at room temperature and then dried using a SpeedVac. For 1 mg AIR, 400 μL of trifluoroacetic acid 2 M (freshly made) was added and incubated at 120 °C for 1 h. After centrifugation at 4 °C during 15 min, the supernatant was used for the injection. The pellet was washed twice with ethanol 70% and then dried. Sixty-three μL of H_2SO_4 72% was added at 20 °C during 1 h, and then, 690 μL of H_2O was added, and the samples were placed 3 h at 100 °C under agitation. After centrifugation at 4 °C during 15 min, the supernatant was used for the injection. Monosaccharide composition of the different supernatant was subsequently determined by high-performance anion exchange chromatography with pulsed amperiometric detection using a PA20 column (Dionex).

Quantification of ^{13}C-glucose incorporation into crystalline cellulose

Twenty mg of sterilized seeds were grown for 3 d in Arabidopsis medium in the dark and under agitation. On the 3rd day, 1% (*w*/*v*) glucose (90% [*w*/*v*] glucose, 10% [*w*/*v*] ^{13}C-glucose, Sigma Cas number: 201136-45-0) was added with DMSO (0.5% [*v*/*v*]) or 50 μM P4B during 5 h or 24 h. After the growth plants were placed into ethanol 96% (*v*/*v*). The cellulose content was performed on an AIR and prepared as described for the analysis of polysaccharide in the previous section. For each sample, 1 μg was carefully weighed in tin capsules to quantify the total ^{13}C percentage using a FLASH 2000 Organic Elemental Analyzer (Thermo Fisher Scientific) coupled to a DELTA V Advantage Isotope Ratio Mass Spectrometer (Thermo Fisher Scientific).

Homogalacturonan enzymatic fingerprinting

AIR were subjected to the endo-polygalacturonase M2 (*Aspergillus aculeatus*), and the oligosaccharides thus produced were analyzed according to Paterlini et al. (2022).

P4B-resistant mutant screening, map-based cloning, and complementation experiment

A total of 100,000 EMS-mutagenized M2 seeds of Col-0 background were germinated and grown on 1/2 MS solid medium containing 50 μM P4B in the dark at 22 °C for 3 d, and P4B-resistant seedlings with longer hypocotyls were selected for further characterization. In order to clone the genetic locus responsible for the chemical resistance of the chemical-resistant mutant, F1 and F2 progenies from the crosses of the P4B-resistant mutant and Ler WT were generated and used. About 1,000 chemical-resistant F2 lines were used to delimit the mutant gene in a 30 kb interval between 5-AB018111-0563 (1.51 Mb) and 5-AB010692-0574 (1.54 Mb) containing 8 candidate genes using all public available InDel and CAPs markers. These genes from both the mutant and WT were sequenced to identify the mutation site.

For complementation experiment, *pCESA3-CESA3* construct was made by using Gateway cloning technology (Invitrogen). A 7.1 kb fragment of the *CESA3* gene containing its native promoter was amplified by PCR. Subsequently, they were introduced in pENTR vector using the pENTR/D-TOPO Cloning Kit (Invitrogen, USA). Then, an LR reaction was performed to clone *pCESA3-CESA3* into the pGWB404 binary vector (Nakagawa et al. 2007). *pCESA3-CESA3* construct was transformed into *Arabidopsis cesa3*^{pbr1} plant through flower dip method (Clough and Bent 1998). Ten transgenic T1 plants were selected on solid medium containing hygromycin (30 μg/mL, Roche). Two T2 lines homozygous for *cesa3*^{pbr1} containing the transgene were fully sensitive to P4B (Fig. 2), while the 8 other transformants were partially or fully P4B-resistant.

Semithin section sample preparation and microscopy

The rice samples for cross-section were prepared as described (Song et al. 2007). Materials of the top, the middle, and the bottom of 3-d-old rice coleoptiles were fixed in FAA (50% [*v*/*v*] ethanol, 5% [*v*/*v*] acetic acid, and 5% [*v*/*v*] formaldehyde) for overnight, dehydrated in an ethanol series, and embedded in Paraplast separately (Sigma). Tissue sections (10 μm thick) were cut with a rotary microtome (RM 2235), mounted, and stained with toluidine blue. Sections were observed and photographed under an AX10 microscope (Zeiss) with a Zeiss Axio camera. *Arabidopsis* hypocotyl transverse semithin sections of each seedling group were stained by toluidine blue and observed using a BX51TRF microscope (Olympus). Images were made using an Olympus DP71 digital camera.

Downloaded from https://academic.oup.com/plphys/article/196/1/124/7687647 by INRA Recherches Forestieres user on 04 September 2024

Transmission electron microscopy observation and measurement of cell wall thickness

Dark-grown Arabidopsis seedlings were collected and fixed in 3% (v/v) paraformaldehyde and 0.5% (v/v) glutaraldehyde in 0.1 M phosphate buffered saline (PBS), pH7.5, with vacuum infiltration for 3 times and stored at 4 °C overnight. After 3 washes with 0.1 M PBS, seedlings were postfixed in 1% osmic acid for 2 h. Then, the tissues were extensively washed using 0.1 M PBS and dehydrated through graded ethanol solutions. The hypocotyl fragments of the elongation zone from aforementioned tissues were dissected and then embedded in LR white resin (Polysciences, Warrington, PA, USA) and polymerized at 50 °C. Transversal ultrathin sections of 100 nm were cut using an ultramicrotome (Ultracut UC6; Leica) and then picked up onto formvar-coated nickel mesh grids. After drying at room temperature, plant sections were stained with periodic acid, thiocarbohydrazide, and silver proteinate (PATAg) for observing the wall polysaccharides as described (Chan et al. 2010). Grids were examined under an electron microscope (H-7650; HITACHI, Kyoto, Japan) at 100 kV. Cell wall thickness was measured using ImageJ software (NIH), and ultrathin sections from 3 hypocotyls of each seedling group were used for observation and measurement.

Spinning disk confocal microscopy

Seedlings expressing GFP-CESA3, GFP-TUA6, EB1a-GFP and dual label lines of GFP-CESA3 and mCherry-MBD were visualized and imaged on an Olympus IX81 confocal microscope equipped with a Yokogawa CSU-X1 spinning disk head, Olympus 100×/1.4 numeral aperture oil objective, and Andor EMCCD iXon Ultra camera (The Core Facility Center, Shanghai Institute of Plant Physiology and Ecology) or on an Axio Observer Z1 Zeiss confocal microscope equipped with a Yokogawa CSU-X1 spinning disk, Zeiss 3100/1.4 numerical aperture oil objective, and Roper EMCCD Quantum 512C (time exposure: 500 ms) (Plateforme d'Imagerie Institut JeanPierre Bourgin-Institut national de recherche pour l'agriculture, l'alimentation et l'environnement, Versailles). GFP was excited at 488 nm (10% laser), and mCherry (20% laser) was excited at 561 nm, while emission was collected using bandpass 488/25 and 568/25 filters (Semrock). For time series observation of GFP-CESA3, the video of CESA3 trajectory was taken every 10 s per picture for 10 min in total. To avoid CMT reorientation of dark-grown hypocotyls caused by light effects, manipulations were performed under green light, and all images were acquired <10 min after samples were mounted between slides. For the EB1a-GFP and GFP-TUA6 time-lapse experiments, images were taken every 1 s or 0.5 s during 2 min in total.

Image analysis

Image analysis was performed using ImageJ software (W.S. Rasband; National Institutes of Health). The Stack Reg (Thevenaz et al. 1998) plugin for ImageJ was performed to correct the focus drift due to the extensive growth of etiolated hypocotyls. To quantify the orientation of CMTs in hypocotyl cells, the percentage of CMTs at a certain angle range was calculated according to the ratio of the number of these CMTs to the total CMTs measured. CMTs at the inner face of hypocotyl epidermal cells were measured using the angle tool in ImageJ according to the orientations relative to hypocotyl growth axis as described (Crowell et al. 2011). Different CMTs angles were classified into following 3 categories: transverse direction (–22.5 to 22.5°), oblique direction (22.5 to 67.5°/–67.5 to –22.5°), and longitudinal direction (67.5 to 90°/–90 to –67.5°). At least 19 cells of different hypocotyls were measured, and in each cell, at least 30 CMTs were quantified and analyzed for each treatment. The moving rate of CESA3 was qualified by using Kymograph analysis as described (Bringmann et al. 2012). In brief, after each group of frames were stacked. Kymographs were made using the multiple Kymograph plugin for ImageJ (http://www.embl.de/eamnet/html/body_kymograph.html), and then, particle velocities were calculated from the slopes of kymographs.

Accession numbers

Sequence data from this article can be found in the *Arabidopsis* Genome Initiative under the following accession numbers: CESA3 (At5G05170), TUA6 (AT4G14960), KOR1 (AT5G49720), EB1a (At3g47690), and MBD (from MAP4 and M72414).

Acknowledgments

We thank Xu Chen (Fujian Agriculture and Forestry University) for kindly providing the seeds of EB1b-GFP and *ktn1-1*. We thank Staffan Persson (University of Copenhagen) for kindly providing the seeds of *pom2/csi1*. We thank Yihua Zhou (Institute of Genetics and Developmental Biology, CAS) for helpful discussions and advice. We thank Haimin Li and Wenbo Li (SIPPE) for experimental support. We thank Xiaoyan Gao and Zhiping Zhang (SIPPE) for technical assistance in electron microscopy, Xiaoshu Gao and Yunxiao He for technical assistance in confocal microscopy, and Jiqin Li and Hua Wang (SIPPE) for technical assistance in semithin section preparation.

Author contributions

H.H., S.V., J.R., and Y.Z. conceived the work and wrote the paper; J.R., S.V., D.L., E.A., and M.U. performed image acquisition and analysis; J.R. and D.L. performed molecular analysis of crosses; D.L., J.L., B.Z., Y.Y., J.S., and Y.Z. performed chemical screen and genetic screen; D.L. performed TEM. E.G., A.M. and A.V. performed CW analysis. S.V. agrees to serve as the author responsible for contact and ensures communication.

Supplementary data

The following materials are available in the online version of this article.

Supplementary Figure S1. Structure–activity relationship of chemical P4B analogs.

Supplementary Figure S2. P4B inhibits Arabidopsis seedling growth.

Supplementary Figure S3. P4B inhibits rice seedling growth.

Supplementary Figure S4. P4B does not affect growth of *E. coli* or *S. cerevisiae*.

Supplementary Figure S5. Long-term treatment with P4B greatly reduced CSC density and motility.

Supplementary Figure S6. P4B does not impact the morphology and the motility of TGN and Golgi fluorescent markers.

Supplementary Figure S7. In the *cesa3^{pbr1}* mutant, 24 h P4B treatment does not alter density nor the velocity of CSCs in the plasma membrane.

Supplementary Figure S8. P4B affects the dynamics of CMTs after 24 h treatment.

Supplementary Figure S9. P4B promotes microtubule reorientation but does not affect microtubule–CSC interaction after 24 h treatment.

Supplementary Figure S10. P4B disturbed the cell wall composition.

Downloaded from https://academic.oup.com/plphys/article/196/1/124/7687647 by INRA Recherches Forestieres user on 04 September 2024

Supplementary Figure S11. Outer wall thickness in elongating Col0 and *cesa3*^{pbr1} hypocotyl epidermis cells.

Supplementary Figure S12. Impact of P4B on hypocotyl growth kinetics for Col0 and *cesa3*^{pbr1}.

Supplementary Table S1. Primers used for mapping and genotyping.

Supplementary Video S1. Representative time-lapse of untreated GFP-CESA3/*cesa3*^{je5}.

Supplementary Video S2. Representative time-lapse of P4B-treated GFP-CESA3/*cesa3*^{je5}.

Supplementary Video S3. Representative time-lapse of untreated EB1a-GFP.

Supplementary Video S4. Representative time-lapse of P4B-treated EB1a-GFP.

Funding

This work was supported by grants from the National Natural Science Foundation of China (31171293 and 31371361), Program of Chinese Academy of Sciences to Y.Z., and from the French National Agency for Research (Agence Nationale de la recherche) (ANR-14-CE34-0010-03 PECTOSIGN project and ANR-ANR20-CE11-0008) grants "Pectosign" and "HOMEOWALL" to H.H. J.R. benefited from a PhD fellowship from Université Paris-Saclay (Ecole Doctorale Sciences du végétal SEVE). The funders had no role in study design, data collection and analysis, decision to publish, or preparation of the manuscript. This work has benefited from the support of Institut Jean-Pierre Bourgin (IJPB) https://ijpb.versailles.inrae.fr/en/department-teams/facilities/presentation. The IJPB benefits from the support of the LabEx Saclay Plant Sciences -SPS (ANR-10-LABX-0040-SPS).

Conflict of interest statement. None declared.

Data availability

All data are incorporated into the article and its online supplementary material.

References

Albersheim P, Darvill A, Roberts K, Sederoff RR, Staehelin LA. *Plant cell walls, from chemistry to biology*. New York, USA: Garland Science; 2012. https://doi.org/10.1201/9780203833476

Barton DA, Vantard M, Overall RL. Analysis of cortical arrays from *Tradescantia virginiana* at high resolution reveals discrete microtubule subpopulations and demonstrate that confocal images of arrays can be misleading. *Plant Cell*. 2008:20(4):982–994. https://doi.org/10.1105/tpc.108.058503

Bischoff V, Cookson SJ, Wu S, Scheible WR. Thaxtomin A affects CESA-complex density, expression of cell wall genes, cell wall composition, and causes ectopic lignification in *Arabidopsis thaliana* seedlings. *J Exp Bot*. 2009:60(3):955–965. https://doi.org/10.1093/jxb/ern344

Brabham C, Lei L, Stork J, Barrett M, Gu Y, DeBolt S. Indaziflam herbicidal action: a potent cellulose biosynthesis inhibitor. *Plant Physiol*. 2014:166(3):1177–1185. https://doi.org/10.1104/pp.114.241950

Bringmann M, Li E, Sampathkumar A, Kocabek T, Hauser MT, Persson S. POM-POM2/CELLULOSE SYNTHASE INTERACTING1 is essential for the functional association of cellulose synthase and microtubules in Arabidopsis. *Plant Cell*. 2012:24(1):163–177. https://doi.org/10.1105/tpc.111.093575

Cano-Delgado A, Penfield S, Smith C, Catley M, Bevan M. Reduced cellulose synthesis invokes lignification and defense responses in *Arabidopsis thaliana*. *Plant J*. 2003:34(3):351–362. https://doi.org/10.1046/j.1365-313x.2003.01729.x

Chan J, Calder G, Fox S, Lloyd C. Cortical microtubule arrays undergo rotary movements in Arabidopsis hypocotyl epidermal cells. *Nat Cell Biol*. 2007:9(2):171–175. https://doi.org/10.1038/ncb1533

Chan J, Calder GM, Doonan JH, Lloyd CW. EB1 reveals mobile microtubule nucleation sites in Arabidopsis. *Nat Cell Biol*. 2003:5(11):967–971. https://doi.org/10.1038/ncb1057. Epub 2003 Oct 12.

Chan J, Crowell E, Eder M, Calder G, Bunnewell S, Findlay K, Vernhettes S, Hofte H, Lloyd C. The rotation of cellulose synthase trajectories is microtubule dependent and influences the texture of epidermal cells in Arabidopsis hypocotyls. *J Cell Sci*. 2010:123-((Pt20)):3490–3495. https://doi.org/10.1242/jcs.074641

Clough SJ, Bent AF. Floral dip: a simplified method for Agrobacterium-mediated transformation of *Arabidopsis thaliana*. *Plant J*. 1998:16(6):735–743. https://doi.org/10.1046/j.1365-313x.1998.00343.x

Crowell EF, Bischoff V, Desprez T, Rolland A, Stierhof Y-D, Schumacher K, Gonneau M, Höfte H, Vernhettes S. Pausing of golgi bodies on microtubules regulates secretion of cellulose synthase complexes in Arabidopsis. *Plant Cell*. 2009:21(4):1141–1154. https://doi.org/10.1105/tpc.108.065334

Crowell EF, Timpano H, Desprez T, Franssen-Verheijen T, Emons A-M, Höfte H, Vernhettes S. Differential regulation of cellulose orientation at the inner and outer face of epidermal cells in the Arabidopsis hypocotyl. *Plant Cell*. 2011:23(7):2592–2605. https://doi.org/10.1105/tpc.111.087338

Cutler SR, Ehrhardt DW, Griffitts JS, Somerville CR. Random GFP::cDNA fusions enable visualization of subcellular structures in cells of *Arabidopsis* at a high frequency. *Proc Natl Acad Sci U S A*. 2000:97(7):3718–3723. https://doi.org/10.1073/pnas.97.7.3718

DeBolt S, Gutierrez R, Ehrhardt DW, Melo CV, Ross L, Cutler SR, Somerville C, Bonetta D. Morlin, an inhibitor of cortical microtubule dynamics and cellulose synthase movement. *Proc Natl Acad Sci U S A*. 2007a:104(14):5854–5859. https://doi.org/10.1073/pnas.0700789104

DeBolt S, Gutierrez R, Ehrhardt DW, Somerville C. Nonmotile cellulose synthase subunits repeatedly accumulate within localized regions at the plasma membrane in Arabidopsis hypocotyl cells following 2,6-dichlorobenzonitrile treatment. *Plant Physiol*. 2007b:145(2):334–338. https://doi.org/10.1104/pp.107.104703

Derbyshire P, Findlay K, McCann MC, Roberts K. Cell elongation in Arabidopsis hypocotyls involves dynamic changes in cell wall thickness. *J Exp Bot*. 2007:58(8):2079–2089. https://doi.org/10.1093/jxb/erm074

Desprez T, Juraniec M, Crowell EF, Jouy H, Pochylova Z, Parcy F, Höfte H, Gonneau M, Vernhettes S. Organization of cellulose synthase complexes involved in primary cell wall synthesis in *Arabidopsis thaliana*. *Proc Natl Acad Sci U S A*. 2007:104(39):15572–15577. https://doi.org/10.1073/pnas.0706569104

Desprez T, Vernhettes S, Fagard M, Refrégier G, Desnos T, Aletti E, Py N, Pelletier S, Höfte H. Resistance against herbicide isoxaben and cellulose deficiency caused by distinct mutations in same cellulose synthase isoform CESA6. *Plant Physiol*. 2002:128(2):482–490. https://doi.org/10.1104/pp.010822

Dettmer J, Hong-Hermesdorf A, Stierhof Y-D, Schumacher K. Vacuolar H+-ATPase activity is required for endocytic and secretory trafficking in *Arabidopsis*. *Plant Cell*. 2006:18(3):715–730. https://doi.org/10.1105/tpc.105.037978

Endler A, Kesten C, Schneider R, Zhang Y, Ivakov A, Froehlich A, Funke N, Persson S. A mechanism for sustained cellulose synthesis during salt stress. *Cell* 2015:162(6):1353–1364. https://doi.org/10.1016/j.cell.2015.08.028

Downloaded from https://academic.oup.com/plphys/article/196/1/124/7687647 by INRA Recherches Forestieres user on 04 September 2024

Geldner N, Dénervaud-Tendon V, Hyman DL, Mayer U, Stierhof Y-D, Chory J. Rapid, combinatorial analysis of membrane compartments in intact plants with a multicolor marker set. *Plant J*. 2009:59(1):169–178. https://doi.org/10.1111/j.1365-313X.2009.03851.x

Gonneau M, Desprez T, Guillot A, Vernhettes S, Höfte H. Catalytic subunit stoichiometry within the cellulose synthase complex. *Plant Physiol*. 2014:166(4):1709–1712. https://doi.org/10.1104/pp.114.250159

Gu Y, Kaplinsky N, Bringmann M, Cobb A, Carroll A, Sampathkumar A, Baskin TI, Persson S, Somerville CR. Identification of a cellulose synthase-associated protein required for cellulose biosynthesis. *Proc Natl Acad Sci U S A*. 2010:107(29):12866–12871. https://doi.org/10.1073/pnas.1007092107

Gutierrez R, Lindeboom JJ, Paredez AR, Emons AM, Ehrhardt DW. Arabidopsis cortical microtubules position cellulose synthase delivery to the plasma membrane and interact with cellulose synthase trafficking compartments. *Nat Cell Biol*. 2009:11(7):797–806. https://doi.org/10.1038/ncb1886

Hamant O, Inoue D, Bouchez D, Dumais J, Mjolsness E. Are microtubules tension sensors? *Nat Commun*. 2019:10(1):2360. https://doi.org/10.1038/s41467-019-10207-y

Harris DM, Corbin K, Wang T, Gutierrez R, Bertolo AL, Petti C, Smilgies D-M, Estevez JM, Bonetta D, Urbanowicz BR, *et al*. Cellulose microfibril crystallinity is reduced by mutating C-terminal transmembrane region residues CESA1A903V and CESA3T942I of cellulose synthase. *Proc Natl Acad Sci U S A*. 2012:109(11):4098–4103. https://doi.org/10.1073/pnas.1200352109

Heim DR, Roberts JL, Pike PD, Larrinua IM. Mutation of a locus of *Arabidopsis thaliana* confers resistance to the herbicide isoxaben. *Plant Physiol*. 1989:90(1):146–150. https://doi.org/10.1104/pp.90.1.146

Himmelspach R, Williamson RE, Wasteneys GO. Cellulose microfibril alignment recovers from DCB-induced disruption despite microtubule disorganization. *Plant J*. 2003:36(4):565–575. https://doi.org/10.1046/j.1365-313x.2003.01906.x

Hu Z, Vanderhaeghen R, Cools T, Wang Y, De Clercq I, Leroux O, Nguyen L, Belt K, Millar AH, Audenaert D, *et al*. Mitochondrial defects confer tolerance against cellulose deficiency. *Plant Cell*. 2016:28(9):2276–2290. https://doi.org/10.1105/tpc.16.00540

Huang L, Li X, Zhang W, Ung N, Liu N, Yin X, Li Y, Mcewan RE, Dilkes B, Dai M, *et al*. Endosidin20 targets the cellulose synthase catalytic domain to inhibit cellulose biosynthesis. *Plant Cell*. 2020:32(7):2141–2157. https://doi.org/10.1105/tpc.20.00202

Kost B, Spielhofer P, Chua N-H. A GFP-mouse talin fusion protein labels plant actin filaments *in vivo* and visualizes the actin cytoskeleton in growing pollen tubes. *Pant J*. 1998:16(3):393–401. https://doi.org/10.1046/j.1365-313x.1998.00304.x

Lampugnani ER, Khan GA, Somssich M, Persson S. Building a plant cell wall at a glance. *J Cell Sci*. 2018:131(2):2. https://doi.org/10.1242/jcs.207373

Larson RT, McFarlane HE. Small but mighty: an update on small molecule plant cellulose biosynthesis inhibitors. *Plant Cell Physiol*. 2021:62(12):1828–1838. https://doi.org/10.1093/pcp/pcab108

Marc J, Granger CL, Brincat J, Fisher DD, Kao T, McCubbin AG, Cyr RJ. A *GFP–MAP4* reporter gene for visualizing cortical microtubule rearrangements in living epidermal cells. *Plant Cell*. 1998:10(11):1927–1939. https://doi.org/10.1105/tpc.10.11.1927

Nakagawa T, Kurose T, Hino T, Tanaka K, Kawamukai M, Niwa Y, Toyooka K, Matsuoka K, Jinbo T, Kimura T. Development of series of gateway binary vectors, pGWBs, for realizing efficient construction of fusion genes for plant transformation. *J Biosci Bioeng*. 2007:104(1):34–41. https://doi.org/10.1263/jbb.104.34

Paredez AR, Somerville CR, Ehrhardt DW. Visualization of cellulose synthase demonstrates functional association with microtubules. *Science* 2006:312(5779):1491–1495. https://doi.org/10.1126/science.1126551

Paterlini A, Sechet J, Immel F, Grison MS, Pilard S, Pelloux J, Mouille G, Bayer EM, Voxeur A. Enzymatic fingerprinting reveals specific xyloglucan and pectin signatures in the cell wall purified with primary plasmodesmata. *Front Plant Sci*. 2022:13:1020506. https://doi.org/10.3389/fpls.2022.1020506

Peaucelle A, Wightman R, Höfte H. The control of growth symmetry breaking in the arabidopsis hypocotyl. *Curr Biol*. 2015:25(13):1746–1752. https://doi.org/10.1016/j.cub.2015.05.022

Pelletier S, Van Orden J, Wolf S, Vissenberg K, Delacourt J, Ndong YA, Pelloux J, Bischoff V, Urbain A, Mouille G, *et al*. A role for pectin de-methylesterification in a developmentally regulated growth acceleration in dark-grown Arabidopsis hypocotyls. *New Phytol*. 2010:188(3):726–739. https://doi.org/10.1111/j.1469-8137.2010.03409.x

Persson S, Paredez A, Carroll A, Palsdottir H, Doblin M, Poindexter P, Khitrov N, Auer M, Somerville CR. Genetic evidence for three unique components in primary cell-wall cellulose synthase complexes in *Arabidopsis*. *Proc Natl Acad Sci U S A*. 2007:104(39):15566–15571. https://doi.org/10.1073/pnas.0706592104

Purushotham P, Ho R, Zimmer J. Architecture of a catalytically active homotrimeric plant cellulose synthase complex. *Science* 2020:369(6507):1089–1094. https://doi.org/10.1126/science.abb2978

Refrégier G, Pelletier S, Jaillard D, Höfte H. Interaction between wall deposition and cell elongation in dark-grown hypocotyl cells in Arabidopsis. *Plant Physiol*. 2004:135(2):959–968. https://doi.org/10.1104/pp.104.038711

Scheible WR, Eshed R, Richmond T, Delmer D, Somerville C. Modifications of cellulose synthase confer resistance to isoxaben and thiazolidinone herbicides in Arabidopsis Ixr1 mutants. *Proc Natl Acad Sci U S A*. 2001:98(18):10079–10084. https://doi.org/10.1073/pnas.191361598

Schneider R, Ehrhardt DW, Meyerowitz EM, Sampathkumar A. Tethering of cellulose synthase to microtubules dampens mechano-induced cytoskeletal organization in Arabidopsis pavement cells. *Nat Plants*. 2022:8(9):1064–1073. https://doi.org/10.1038/s41477-022-01218-7

Shim I, Law R, Kileeg Z, Stronghill P, Northey JGB, Strap JL, Bonetta DT. Alleles causing resistance to isoxaben and flupoxam highlight the significance of transmembrane domains for CESA protein function. *Front Plant Sci*. 2018:9:1152. https://doi.org/10.3389/fpls.2018.01152

Song XJ, Huang W, Shi M, Zhu MZ, Lin HX. A QTL for rice grain width and weight encodes a previously unknown RING-type E3 ubiquitin ligase. *Nat Genet*. 2007:39(5):623–630. https://doi.org/10.1038/ng2014

Surpin M, Rojas-Pierce M, Carter C, Hicks GR, Vasquez J, Raikhel NV. The power of chemical genomics to study the link between endomembrane system components and the gravitropic response. *Proc Natl Acad Sci U S A*. 2005:102(13):4902–4907. https://doi.org/10.1073/pnas.0500222102

Tateno M, Brabham C, DeBolt S. Cellulose biosynthesis inhibitors—a multifunctional toolbox. *J Exp Bot*. 2016:67(2):533–542. https://doi.org/10.1093/jxb/erv489

Thevenaz P, Ruttimann UE, Unser M. A pyramid approach to subpixel registration based on intensity. *IEEE Trans Image Process*. 1998:7(1):27–41. https://doi.org/10.1109/83.650848

Vain T, Crowell EF, Timpano H, Biot E, Desprez T, Mansoori N, Trindade LM, Pagant S, Robert S, Höfte H, *et al*. The cellulase KORRIGAN is

Downloaded from https://academic.oup.com/plphys/article/196/1/124/7687647 by INRA Recherches Forestieres user on 04 September 2024

part of the cellulose synthase complex. *Plant Physiol.* 2014:165(4): 1521–1532. https://doi.org/10.1104/pp.114.241216

Worden N, Wilkop TE, Esteve VE, Jeannotte R, Lathe R, Vernhettes S, Weimer B, Hicks G, Alonso J, Labavitch J, *et al.* CESA TRAFFICKING INHIBITOR inhibits cellulose deposition and interferes with the trafficking of cellulose synthase complexes and their associated proteins KORRIGAN1 and POM2/CELLULOSE SYNTHASE INTERACTIVE PROTEIN1. *Plant Physiol.* 2015:167(2):381–393. https://doi.org/10.1104/pp.114.249003

Xia Y, Lei L, Brabham C, Stork J, Strickland J, Ladak A, Gu Y, Wallace I, DeBolt S. Acetobixan, an inhibitor of cellulose synthesis identified by microbial bioprospecting. *PLoS One* 2014:9(4):e95245. https://doi.org/10.1371/journal.pone.0095245

Yoneda A, Higaki T, Kutsuna N, Kondo Y, Osada H, Hasezawa S, Matsui M. Chemical genetic screening identifies a novel inhibitor of parallel alignment of cortical microtubules and cellulose microfibrils. *Plant Cell Physiol.* 2007:48(10):1393–1403. https://doi.org/10.1093/pcp/pcm120

Zhao Y, Chow TF, Puckrin RS, Alfred SE, Korir AK, Larive CK, Cutler SR. Chemical genetic interrogation of natural variation uncovers a molecule that is glycoactivated. *Nat Chem Biol.* 2007:3(11):716–721. https://doi.org/10.1038/nchembio.2007.32

Zhu Y, McFarlane HE. Regulation of cellulose synthesis via exocytosis and endocytosis. *Curr Opin Plant Biol.* 2022:69:102273. https://doi.org/10.1016/j.pbi.2022.102273

Downloaded from https://academic.oup.com/plphys/article/196/1/124/7687647 by INRA Recherches Forestieres user on 04 September 2024